The Astrophysical Journal Letters, 889:L2 (7pp), 2020 January 20 https://doi.org/10.3847/2041-8213/ab64d0

Case Study of Solar Wind Suprathermal Electron Acceleration at the Earth's Bow Shock

Zixuan Liu[1], Linghua Wang[1], Quanqi Shi[2], Mitsuo Oka[3], Liu Yang[1], Robert F. Wimmer-Schweingruber[4], Jiansen He[1], Hui Tian[1], and Stuart D. Bale[5]

[1] School of Earth and Space Sciences, Peking University, Beijing, 100871, People's Republic of China; wanglhwang@gmail.com, wanglhwang@pku.edu.cn
[2] Shandong Key Laboratory of Optical Astronomy and Solar-Terrestrial Environment, School of Space Science and Physics, Institute of Space Sciences, Shandong University, Weihai, Shandong, 264209, People's Republic of China
[3] Space Sciences Laboratory, University of California, Berkeley, CA 94720, USA
[4] Institute of Experimental and Applied Physics, University of Kiel, Leibnizstrasse 11, D-24118 Kiel, Germany
[5] Department of Physics and Space Sciences Laboratory, University of California, Berkeley, CA 94720, USA
Received 2019 October 25; revised 2019 November 16; accepted 2019 December 21; published 2020 January 17

Abstract

We present a case study of the in situ acceleration of solar wind suprathermal electrons at the two quasi-perpendicular-bow-shock crossings on 2015 November 4, combining the *Wind* 3D Plasma and Energetic Particle measurements of ambient solar wind suprathermal electrons and *Magnetospheric Multiscale* mission measurements of shocked suprathermal electrons. In both cases, the omnidirectional differential fluxes of shocked suprathermal electrons in the downstream exhibit a double-power-law energy spectrum with a spectral index of ∼3 at energies below a downward break $\varepsilon_{\rm brk}$ near 40 keV and index of ∼6 at energies above, different from the unshocked suprathermal electrons observed in the ambient solar wind. At energies below (above) $\varepsilon_{\rm brk}$, the observed electron flux ratio between the downstream and ambient solar wind, J_D/J_A, peaks near 90° PA (becomes roughly isotropic). Electrons at $\varepsilon_{\rm brk}$ have an average electron gyrodiameter (across bow shock) comparable to the shock thickness. These suggest that the bow-shock acceleration of suprathermal electrons is likely dominated by the shock drift acceleration mechanism. For electrons at energies below (above) $\varepsilon_{\rm brk}$, their estimated drift time appears to be roughly energy independent (decrease with energy), leading to the formation of a double-power-law spectrum substantially steepening at a break that's determined by the shock thickness.

Unified Astronomy Thesaurus concepts: Shocks (2086)

1. Introduction

Many theoretical studies have proposed two major shock acceleration mechanisms (e.g., Kallenrode 2013; Desai & Giacalone 2016): first-order-Fermi shock acceleration (FFA) and shock drift acceleration (SDA) that are thought to be more efficient, respectively, under quasi-parallel and quasi-perpendicular shock geometries. In FFA, charged particles can gain energy via multiple reflections/scatterings between converging upstream and downstream waves (e.g., Fisk 1971; Desai & Giacalone 2016; Oka et al. 2019), while in SDA, charged particles can be energized through gradient B drift along the $-\vec{U} \times \vec{B}$ induced electric field at the shock surface for both reflection and transmission (e.g., Decker 1992; Ball & Melrose 2001). In a steady state, the FFA mechanism predicts a power-law spectrum of accelerated particles in the form of $J \propto \varepsilon^{-\beta}$ with a spectral index of $\beta = (r+2)/(2r-2)$ (e.g., Drury 1983; Van Nes et al. 1984), where J is the differential particle flux and r is the shock density compression ratio. Recent studies suggest that FFA and SDA can be incorporated under the theory of diffusive shock acceleration (Desai & Giacalone 2016; Qin et al. 2018).

Suprathermal electrons in the solar wind (e.g., Maksimovic et al. 2005; Wang et al. 2012; Tao et al. 2016) can provide seed particles for electron acceleration at interplanetary shocks and planetary bow shocks. At 1 au, in situ measurements show that electron acceleration occurs more efficiently at quasi-perpendicular geometries rather than at quasi-parallel geometries (e.g., Tsurutani & Lin 1985; Shimada et al. 1999; Yang et al. 2018), for both the terrestrial bow shock and interplanetary shocks. Using Geotail electron measurements, Oka et al. (2006) found that shocked suprathermal electrons at bow shock show a single-power-law spectrum at ∼0.2–10 keV with a spectral index of $\beta \sim$ 2–4, consistent with *ISEE 1* and *2* measurements (Gosling et al. 1989). Utilizing high-sensitivity electron measurements by the *Wind* 3D Plasma and Energetic Particle (3DP) instrument across interplanetary shocks, Yang et al. (2018, 2019) reported that the downstream suprathermal electrons (when significantly shocked) generally have a double-power-law spectrum with a $\beta \sim$ 2–6 at energies below an upward break near 1–2 keV and a $\beta \sim$ 2–3 at energies above, similar to the ambient unshocked suprathermal electrons. They suggested that the SDA plays a more important role in accelerating electrons at interplanetary shocks, with an electron drift time along the shock on the order of ∼0.5–2 s.

In this Letter, we present a case study of electron acceleration over a broad energy range at the terrestrial bow shock, combining the *Wind* 3DP measurements of ambient solar wind suprathermal electrons and *Magnetospheric Multiscale* (*MMS*) mission measurements of shocked suprathermal electrons.

2. Observations

The *MMS* mission (*MMS1*, *MMS2*, *MMS3*, and *MMS4*; Burch et al. 2016) was launched on 2015 March 12 into an elliptical Earth orbit with an apogee ranging from 12 $R_{\rm E}$ to 25 $R_{\rm E}$ (Fuselier et al. 2016). The onboard Fast Plasma Investigation (FPI) measures the electron and ion velocity distributions at energies from 10 eV to 30 keV (Pollock et al. 2016), while the Fly's Eye Energetic Particle Spectrometer (FEEPS) measures the electron distributions at 25–650 keV (Blake et al. 2016). The three-dimensional electron data from FPI and FEEPS are binned into pitch-angle (PA) bins according to the direction of magnetic field measured by the Fluxgate Magnetometer (Torbert et al. 2016).

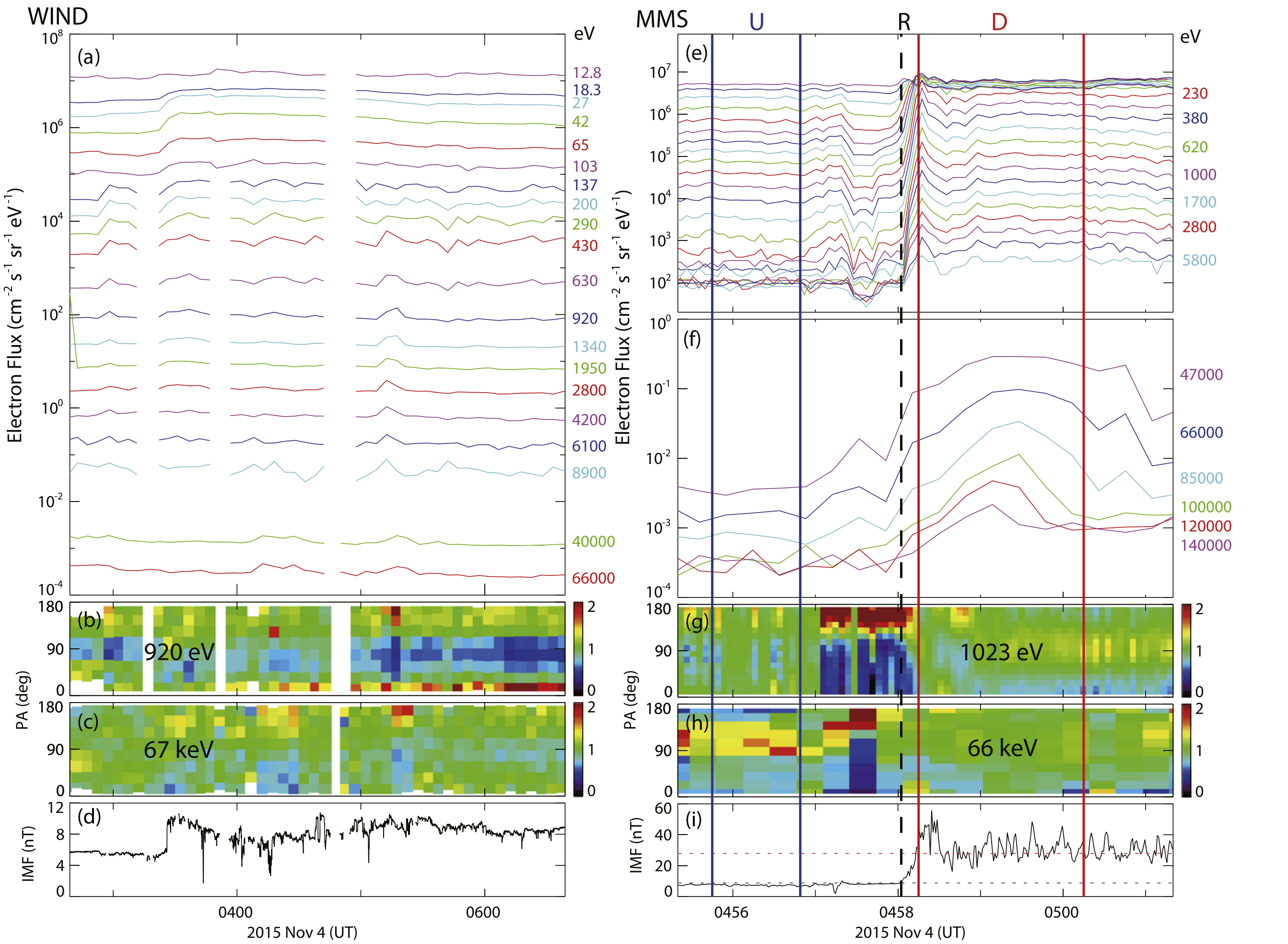

Figure 1. Left panels: *Wind* measurements around L1 at 0239–0639 UT on 2015 November 4. (a) Omnidirectional electron fluxes at ∼10 eV to ∼66 keV. (b)–(c) Electron PADs at 920 eV and 66 keV, normalized by the PA-average flux for each time bin. (d) IMF magnitude. Right panels: *MMS1* measurements of a bow-shock crossing near 0458 UT (Case 1). The upstream (downstream) is sampled by an interval between the vertical blue lines (vertical red lines), and the ramp is defined by an interval between the vertical black dashed line and the left vertical red line. (e)–(f) Omnidirectional electron fluxes measured by FPI at ∼20 eV to 5.8 keV and by FEEPS at ∼47 keV to 520 keV. (g)–(h) Electron PADs at 1 and 66 keV, normalized by the PA-average flux for each time bin. (j) IMF magnitude.

The *Wind* spacecraft has remained in halo orbits around the Sun–Earth L1 point since mid-2004 May (Wang 2009). In the onboard 3DP instrument (Lin et al. 1995), the electron electrostatic analyzers (EESA-L and EESA-H) measure the full three-dimensional electron distributions from solar wind plasma to 30 keV, while silicon semiconductor telescopes measure ∼25–400 keV electron velocity distributions. The three-dimensional electron data from 3DP are binned into eight PA bins with a 22°.5 angular resolution (Wang 2009), according to the direction of the interplanetary magnetic field (IMF) measured by the *Wind* Magnetic Field Investigation (MFI) instrument (Lepping et al. 1995).

In this study, we examine the transition of energy spectrum and PA distribution (PAD) of solar wind suprathermal electrons from the ambient solar wind through the terrestrial bow shock into its downstream, after combining high-sensitivity electron measurements over a wide energy range of a few eV to ∼500 keV from *Wind* and *MMS*. On 2015 November 4, the *MMS* spacecraft crossed the bow shock more than 10 times as the bow shock rapidly moved in and out. We use the *MMS1* measurements to study the solar wind plasma and suprathermal electrons across the bow shock, since the four *MMS* spacecraft was separated only by $\lesssim$10 km, much smaller than the scale of the bow shock. We utilize the high-sensitivity *Wind*/3DP measurements to study the suprathermal electrons in the ambient solar wind. Among these shock crossings, we select one crossing at 0458 UT (also see Oka et al. 2019) with the strongest electron flux measured at 140 keV in downstream (Case 1) and one crossing at 0439 UT with the strongest 140 keV electron flux in upstream (Case 2) near the bow shock. For both cases, we obtain the shock parameters (the shock's normal unit vector $\hat{n}_{sh}$, normal velocity V_{sh}, angle θ_{Bn} between the shock's normal and upstream IMF, fast magnetosonic Mach number M_f, and r) from the nonlinear least-square shock fitting techniques (Szabo 1994; Koval & Szabo 2008), while the timing analysis of four *MMS* spacecraft measurements (Schwartz 1998) gives an unreasonable estimate of $V_{sh} \sim 300$–$500\ \mathrm{km\ s^{-1}}$ (probably due to a short spacecraft separation). For Case 1 (2), the fitted parameters are $\theta_{Bn} = 81°.1 \pm 2°.5$ ($79°.2 \pm 5°.2$), $V_{sh} = 11.9 \pm 4.6\ \mathrm{km\ s^{-1}}$ ($16.6 \pm 6.9\ \mathrm{km\ s^{-1}}$), $M_f = 4.55 \pm 0.14$ (3.87 ± 0.28), and $r = 3.73 \pm 0.19$ (3.73 ± 0.38).

On 2015 November 4 (Figure 1), the IMF generally points antisunward from upstream to downstream of the bow shock, and suprathermal electrons measured in the ambient solar wind by *Wind*/3DP show no strong temporal variation. For the two selected bow-shock-crossing cases, we use a 4 hr interval

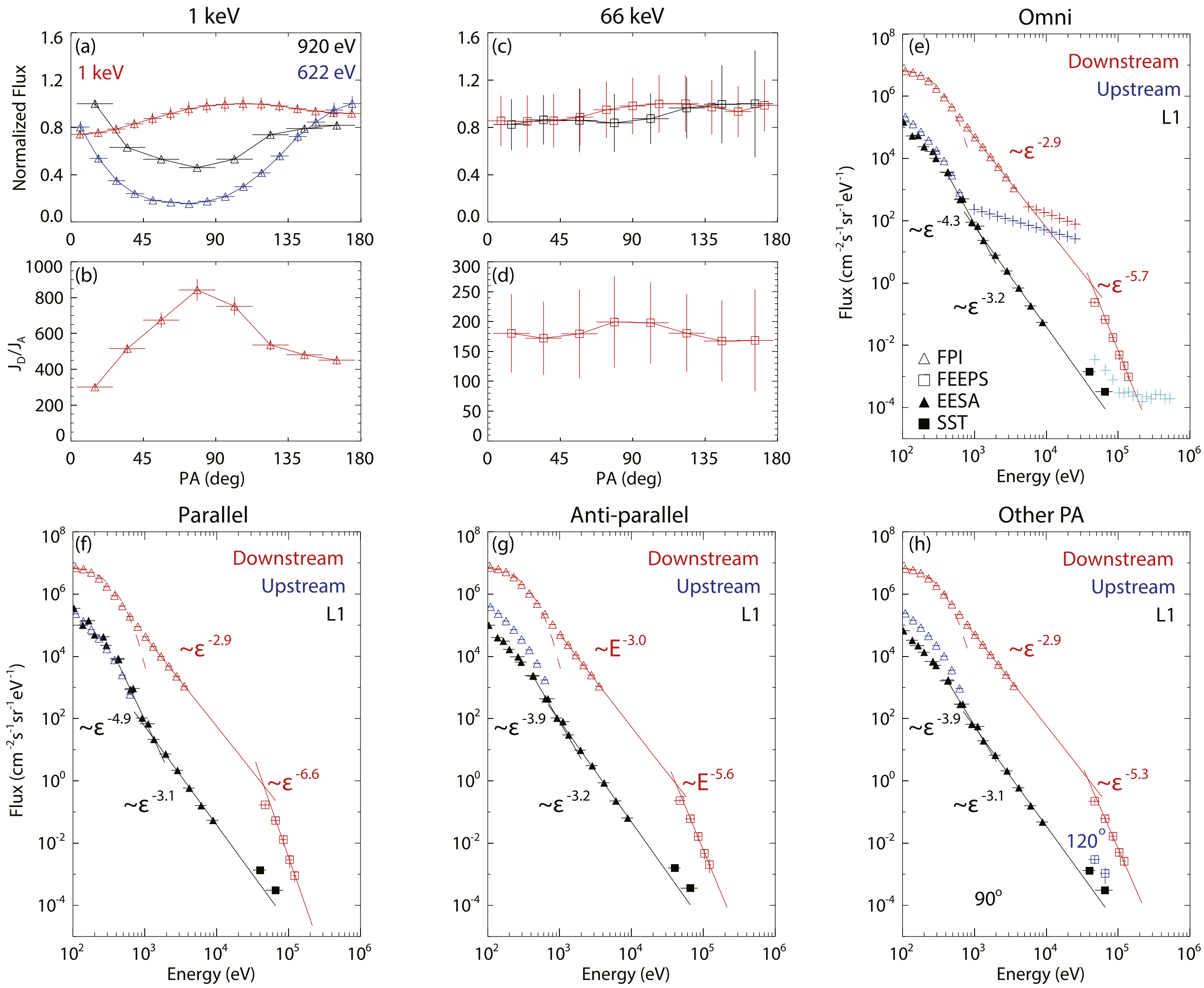

Figure 2. Electron PADs and energy spectra averaged in the ambient solar wind (black symbols), bow shock's near upstream (blue symbols) and downstream (red symbols) for Case 1. (a) Normalized electron PADs near 1 keV. (b) J_D/J_A at 920 eV. (c)–(d) Normalized electron PADs and J_D/J_A at 66 keV. (e) Omnidirectional electron energy spectra. (f)–(g) Energy spectra of electrons at 0°–45° PA (parallel) and 135°–180° PA (antiparallel). (h) Energy spectra of ambient and downstream electrons at 67.°5–112.°5 PA and of upstream electrons at 105°–135° PA. In (e), blue and red crosses show the noise/background of FPI, respectively, in upstream and downstream; light blue crosses show the noise/background of FEEPS.

(0230 UT–0630 UT) to average the ambient solar wind suprathermal electron measurements. The ambient suprathermal electrons mainly consist of an antisunward strahl population beaming along 0° PA and a roughly isotropic halo population at ~0.1–2 keV, plus a roughly isotropic superhalo population at energies above ~2 keV (Wang et al. 2012, 2015). These ambient populations likely represent the seed electrons injected into the bow-shock acceleration. At energies up to 6 keV, these ambient suprathermal electrons also show a sunward population beaming along 180° PA, due to the reflection of solar wind suprathermal electrons at the bow shock and/or escape of shocked suprathermal electrons. After removal of instrumental background due to penetrating particles (Wang et al. 2012), the differential fluxes of ambient suprathermal electrons at ~0.4–80 keV, J_A, can fit to a double-power-law energy spectrum bending upward at a break around 1.5 keV (Figure 2), consistent with previous studies (Wang et al. 2012; Yang et al. 2019). For the omnidirectional fluxes, the fitted spectral index is 4.3 at energies below the break and 3.2 at energies above.

For both bow-shock-crossing cases (Figures 1 and 3), the IMF measured by *MMS1* shows a well-defined shock ramp—the transition from upstream to downstream. We select a 1 minute interval with relatively stable electron fluxes measured at energies below 30 keV in upstream close to the bow shock to calculate the average upstream measurements from *MMS1*, and we select a 2 minute interval starting about 3 minutes after the shock passage to obtain the average far-downstream IMF. According to the typical quasi-perpendicular shock structure described by Hellinger (2003), we define the ramp as an interval in the magnetic field rising phase between a lower threshold (equal to 1.2 times the average upstream IMF; see the horizontal blue dotted line) and upper threshold (equal to the average far-downstream IMF; see the horizontal red dotted line). The bow shock's ramp thickness is defined as $D_{\rm ramp} = |\hat{n}_{\rm sh} \cdot (\overrightarrow{V_{\rm sh}} - \overrightarrow{V_{\rm sc}})|\Delta t$, where Δt is the time duration of shock ramp and $\overrightarrow{V_{\rm sh}}$ ($\overrightarrow{V_{\rm sc}}$) is the velocity of shock (spacecraft). The estimated $D_{\rm ramp}$ is ~100 km for both cases, consistent with the statistical studies (Russell et al. 1982). Afterward, we use a

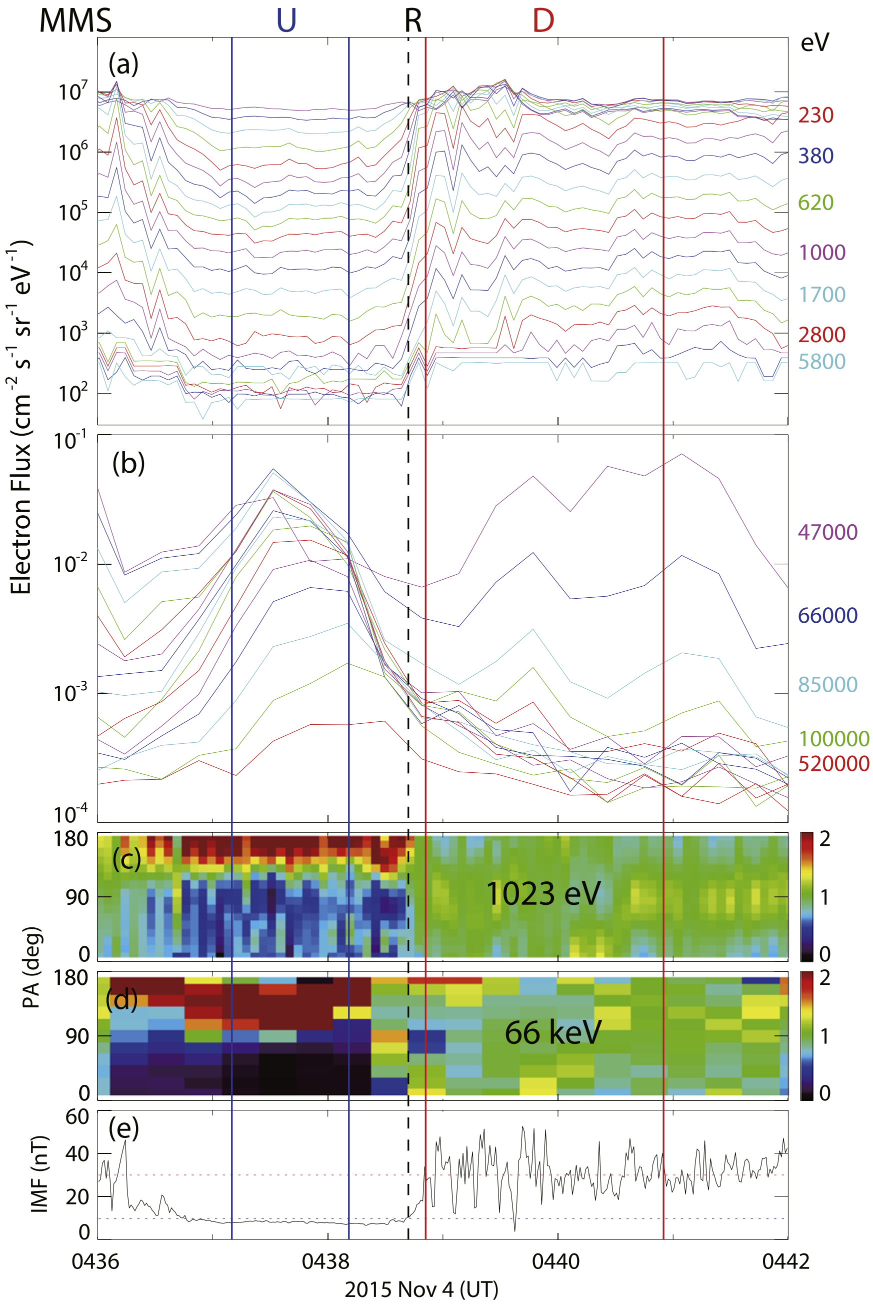

Figure 3. *MMS1* measurements of a bow-shock crossing near 0439 UT (Case 2). Same legend as the right panels of Figure 1.

2 minute time interval adjacent to the ramp to obtain the average downstream measurements, likely reflecting the shocked suprathermal electrons.

In this study, we define that the electron flux measurements, with an intensity at least 5 times higher than the thermal Maxwellian distribution determined by the measured solar wind electron temperature (see the red dashed lines in Figures 2 and 4, for example) are dominated by suprathermal/nonthermal electrons. Then we obtain the suprathermal/nonthermal electron flux (J_A in ambient solar wind and J_D in downstream) after subtracting an isotropic thermal Maxwellian distribution.

2.1. Case 1 with Shock Crossing near 0458 UT

In upstream (Figures 1 and 2), the *MMS1* measurements are dominated by electrons, at energies below 1 keV (at ~40–75 keV) in all PA directions (around 120° PA); those at other energies and/or PAs are dominated by instrumental noise and/or background (see the blue and light blue crosses in Figure 2(e)), higher than the ambient solar wind electron fluxes measured by *Wind*/3DP at L1 (black symbols). At ~0.1–0.9 keV, the *MMS1* upstream suprathermal electrons have an antisunward strahl population beaming along 0° PA and a roughly isotropic halo population (Figure 2(a)), consistent with the ambient suprathermal electrons. At ~0.1–0.9 keV (~40–75 keV), the upstream electrons show a strong sunward population with a PAD peaking near 180° PA (120° PA) and an intensity roughly increasing as approaching to the bow shock (Figures 1(h) and 2(a)), probably due to escape of shocked strahl electrons (reflection of superhalo electrons).

At the start of the shock ramp, solar wind suprathermal electrons show an abrupt increase in flux and decrease in PA anisotropy, at energies up to 150 keV (Figures 1(e)–(h)).

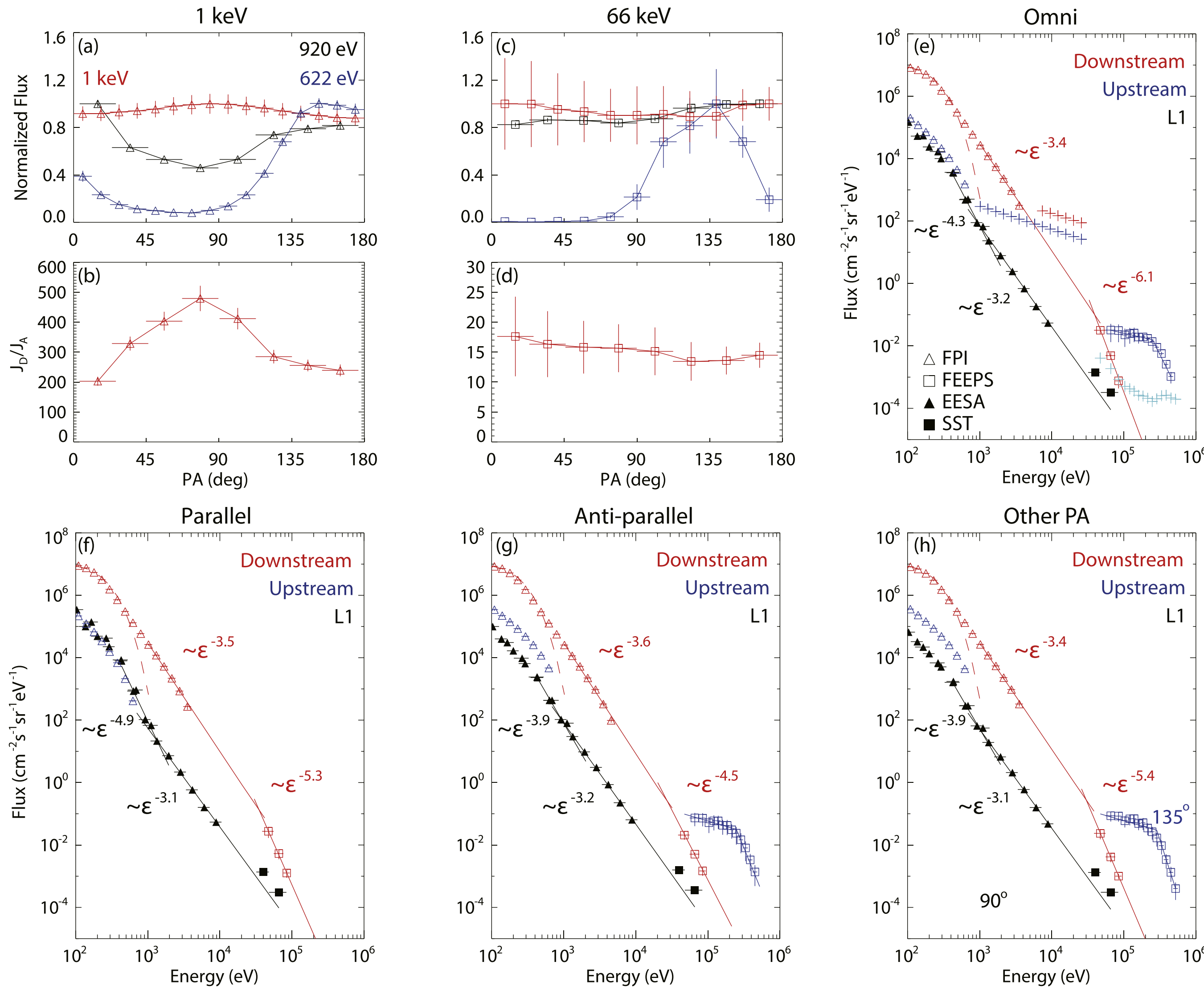

Figure 4. Electron PADs and energy spectra for Case 2. Same legend as Figure 2.

In downstream, these electrons reach a flux maximum shortly after the shock ramp at energies below ~6 keV and exhibit a gradual flux increase at ~40–150 keV, while the *MMS1* measurements at energies between are dominated by instrumental noise/background (see red crosses in Figure 2(e)). In addition, the downstream electron PADs become roughly isotropic at all energies.

At energies above ~0.7 keV, the downstream electrons are dominated by nonthermal electrons. At these suprathermal energies, the omnidirectional electron flux enhancement between the downstream and ambient, J_D/J_A, varies with energy from ~200 to 1400 (Figures 2(b) and (d)), indicating the presence of strong electron acceleration at the bow shock. On the other hand, the downstream suprathermal electrons in all PA directions exhibit a double-power-law energy spectrum, $J_D \propto \varepsilon^{-\beta}$, that bends down at a break of $\varepsilon_{\rm brk} \simeq 40$ keV, different from the ambient suprathermal electrons (Figures 2(e)–(h)). For the omnidirectional fluxes, the fitted spectral index β is ~2.9 at ~0.7–6 keV and is ~5.7 at ~40–150 keV, both significantly larger than the FFA prediction of $\beta_{\rm FFA} = 1.05$. At energies below ~6 keV, J_D/J_A clearly peaks near 90° PA, suggesting that the strongest acceleration occurs in a nearly perpendicular direction.

2.2. Case 2 with Shock Crossing near 0439 UT

In upstream (Figures 3 and 4), the *MMS1* measurements are dominated by electrons, at energies below 1 keV (at ~40–75 keV) in all PA directions (sunward-traveling PA directions during ~0436–0439 UT). At ~0.1–0.9 keV, the *MMS1* upstream suprathermal electrons show a weak antisunward strahl population beaming along 0° PA and a roughly isotropic halo population (Figure 4(a)), equivalent to the ambient suprathermal electrons measured by *Wind* at L1; these electrons also show a strong sunward population that peaks around 140° PA, probably due to reflection and acceleration of strahl electrons at the bow shock. At ~0.9–40 keV, the *MMS1* upstream measurements (see the blue crosses in Figure 4) are dominated by the instrumental noise and/or background. At ~40–560 keV, the sunward-traveling electrons (away from the shock) measured during ~0436–0439 UT exhibit a flux peak occurring earlier at lower energies (i.e., an inverse velocity dispersion), a ~40°-loss-cone PAD (Figures 3(d) and 4(c)), and a possible double-power-law spectrum with a spectral

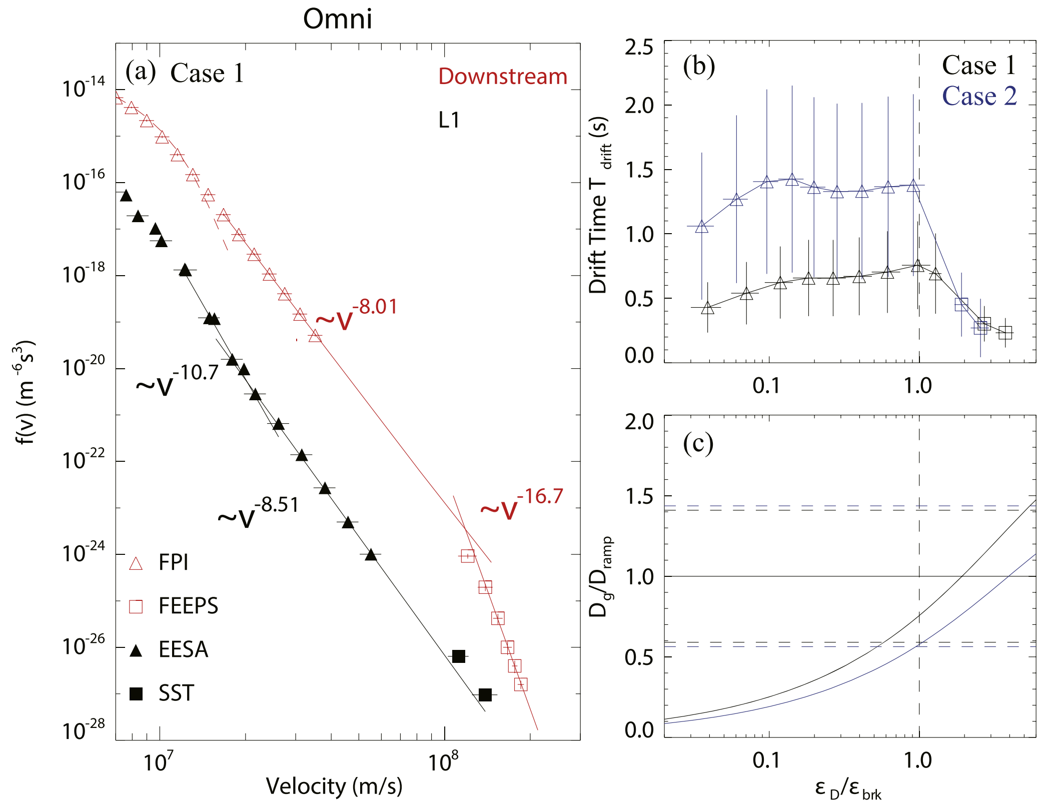

Figure 5. (a) Omnidirectional electron velocity distribution function averaged in the ambient solar wind (in black) and bow shock's downstream (in red) for Case 1. (b)–(c) The estimated $T_{\rm drift}$ and D_g (in unit of $D_{\rm ramp}$) vs. downstream electron energy (in unit of $\varepsilon_{\rm brk}$), for Case 1 (black) and 2 (blue). The horizontal dashed lines show the upper and lower bound of the $D_{\rm ramp}$ estimate.

index of 0.5 at energies below a ∼300 keV and index of 8 at energies above (Figure 4(h)), hereinafter referred to as an "upstream event." This upstream event may be due to suprathermal electrons that are reflected and effectively energized near the tangent point of IMF and bow shock (not the local shock location; e.g., Wu 1984; Krauss-Varban & Wu 1989).

At energies up to ∼6 keV, the *MMS1* electron fluxes increase abruptly at the start of shock ramp and reach a maximum shortly after the ramp, while the electron fluxes at ∼40–110 keV exhibit a gradual peak (Figures 3(a) and (b)), weaker than the upstream event. At energies of ∼6–40 keV or above 110 keV, the *MMS1* downstream measurements are again dominated by instrumental noise/background (see the red crosses in Figure 4(e)). In addition, the downstream electrons are roughly isotropic in PAD at all energies, similar to Case 1.

At energies above ∼0.8 keV, the downstream electrons dominantly consist of nonthermal populations. The omnidirectional J_D/J_A varies with energy from ∼20 to ∼600, while J_D/J_A clearly peaks near 90° PA (is roughly isotropic) at energies below ∼6 keV (at ∼40–110 keV). Furthermore, the downstream suprathermal electrons in all PA directions also have a double-power-law energy spectrum bending downward at $\varepsilon_{\rm brk} \simeq 40$ keV, different from both the ambient suprathermal electrons and upstream event. For the omnidirectional fluxes, the fitted β is ∼3.4 at ∼0.9–6 keV and ∼5.4 at ∼40–110 keV, both significantly larger than the FFA prediction of $\beta_{\rm FFA} = 1.05$.

3. SDA Estimate

For both cases, the shocked suprathermal electrons have spectral indexes significantly larger than the FFA prediction, and the observed J_D/J_A clearly peaks near 90° PA at energies below the spectral break. These results suggest that the bow-shock acceleration of solar wind suprathermal electrons likely favors the SDA theory in which electrons gain energy through gradient-$|B|$ drift along the induced electric field $\vec{E} = -\vec{U} \times \vec{B}$ at shock. The estimated $|\vec{E}|$ is ∼5 mV m^{-1}.

In this study, we use the *Wind* 3DP measurements at L1 to represent seed electrons injected into SDA. As suggested by previous studies of in situ electron acceleration at interplanetary shocks (Yang et al. 2018, 2019), we estimate the electron drift length $L_{\rm drift}$ and drift time $T_{\rm drift}$ in SDA at bow shock, by assuming that solar wind suprathermal electrons remain the same phase space density after acceleration (Liouville's theorem), i.e., $f_D(v_D) = f_A(v_A)$, where f_A (f_D) is the electron phase space density in the ambient solar wind (downstream) before (after) the SDA. For the ambient electrons with a given v_A (Figure 5(a)), we can identify their velocity after acceleration, v_D, to obtain the energy gain $\Delta\varepsilon$, drift length $L_{\rm drift} = \Delta\varepsilon / q|\vec{E}|$, and drift time $T_{\rm drift} = L_{\rm drift}/v_{\rm drift}$ along the $\vec{E}$ at bow shock. The electron gradient drift speed at bow shock is defined as $v_{\rm drift} = (v_{\rm drift}^{\rm up} + v_{\rm drift}^{\rm dn})/2$.

Figure 5 plots the estimated $T_{\rm drift}$ and average electron gyrodiameter, $D_g = R_g^{\rm up} + R_g^{\rm dn}$, where $R_g^{\rm up}$ ($R_g^{\rm dn}$) is the electron gyroradius in upstream (downstream) before (after) SDA. We note that the downstream $\varepsilon_{\rm brk}$ (near 40 keV) corresponds to a $D_g \approx$ the bow shock's ramp thickness $D_{\rm ramp}$. For the suprathermal electrons at energies below $\varepsilon_{\rm brk}$, their D_g is less than $D_{\rm ramp}$ and thus they would experience an efficient trapping and acceleration at shock, characterized by a roughly energy independent $T_{\rm drift}$ in a scale of ∼0.5–2 s. For the shocked electrons at energies above $\varepsilon_{\rm brk}$, however, their D_g is larger than

$D_{\rm ramp}$ and they undergo an inefficient trapping and acceleration, corresponding to a $T_{\rm drift}$ that decreases with energy. Therefore, the shocked suprathermal electrons show a double-power-law spectrum substantially steepening at an $\varepsilon_{\rm brk}$ that's likely determined by $D_{\rm ramp}$.

4. Summary and Discussion

We examine the acceleration of solar wind suprathermal electrons at two quasi-perpendicular-bow-shock crossings with a density compression ratio around 3.7 on 2015 November 4. In both shock-crossing cases, the omnidirectional differential fluxes of downstream suprathermal electrons exhibit a double-power-law energy spectrum of $J \propto \varepsilon^{-\beta}$ with a spectral index of $\beta \sim 3$ at energies below an $\varepsilon_{\rm brk}$ near 40 keV and of $\beta \sim 6$ at energies above, significantly different from unshocked suprathermal electrons in the ambient solar wind. At energies below (above) $\varepsilon_{\rm brk}$, the observed J_D/J_A peaks near 90° PA (become roughly isotropic), with an omnidirectional value ranging from ~400 to ~1400 (from ~20 to ~300). These results suggest that the bow-shock acceleration of solar wind suprathermal electrons is likely dominated by the SDA mechanism.

For both cases, we utilize the electron measurements by *Wind*/3DP at L1 to represent the seed particles for the bow-shock acceleration. We find that the omnidirectional J_D is strongly enhanced by a factor of ~20 to ~1400, compared to J_A. In addition, J_D in all PA directions appears to fit well to a double-power-law energy spectrum bending downward at $\varepsilon_{\rm brk}$ ~40 keV (Figures 2 and 4), significantly different from the ambient suprathermal electron spectrum that bends upward at ~1.5 keV. These results provide evidence for the presence of strong in situ electron acceleration at quasi-perpendicular bow shock.

In Case 1 (2), the fitted downstream β ranges from 2.9 to 3.0 (from 3.4 to 3.6) at energies below $\varepsilon_{\rm brk}$, consistent with that of ~0.2–10 keV electrons observed by Geotail at bow shock (Oka et al. 2006), and β ranges from 5.3 to 6.6 (from 4.5 to 6.1) at energies above. These β are greatly larger than the FFA theoretical prediction of 1.05. On the other hand, J_D/J_A clearly peaks near 90° PA at energies below $\varepsilon_{\rm brk}$, indicating the occurrence of the strongest electron shock acceleration in the direction perpendicular to the IMF, consistent with suprathermal electrons observed by *ISEE 1* and *2* (Gosling et al. 1989). These suggest that the electron bow-shock acceleration in both cases favors the SDA process, consistent with the electron acceleration observed at interplanetary shocks near 1 au (Yang et al. 2018, 2019).

Under assumption that the phase space density of suprathermal electrons is conserved during the SDA (Yang et al. 2018, 2019), we can obtain the electron drift time $T_{\rm drift}$ along the induced $\vec{E}$ and average electron gyrodiameter D_g at the bow shock, as a function of the electron energy in downstream. For both cases, we note that the fitted $\varepsilon_{\rm brk}$ corresponds to an average electron gyrodiameter $D_g \sim 100$ km, comparable to the estimated bow shock's thickness $D_{\rm ramp}$. At energies below (above) $\varepsilon_{\rm brk}$, the estimated $T_{\rm drift}$ appears to be roughly energy independent (to decrease with energy), characteristic of an efficient (inefficient) trapping/acceleration at shock (Yang et al. 2019). Such an SDA efficiency difference between low and high energies likely leads to the formation of a double-power-law spectrum of downstream suprathermal electrons bending downward at an $\varepsilon_{\rm brk}$ determined by $D_{\rm ramp}$.

We would like to thank Drew Turner for helpful discussions on *MMS* observations. This research at Peking University is supported in part by NSFC under contracts 41774183, 41861134033, 41421003, 41574168, 41874200, and in part by ISSI-BJ and ISSI through the international teams 469 and 425. The work at Shandong University is supported by NSFC under contracts 41961130382 and 41974189. R.F.W.S. thanks the German space agency DLR for support under grants 50 OT 1201, 50 OT 1501, and 50 OT 1701. S.B. is supported in part by NASA grants NNX13AL11G and NNX14AC07G. M.O. was supported by NASA grants 80NSSC18K1002, 80NSSC18K1373, and NNH16AC60I.

ORCID iDs

Linghua Wang https://orcid.org/0000-0001-7309-4325
Mitsuo Oka https://orcid.org/0000-0003-2191-1025
Robert F. Wimmer-Schweingruber https://orcid.org/0000-0002-7388-173X
Jiansen He https://orcid.org/0000-0001-8179-417X
Hui Tian https://orcid.org/0000-0002-1369-1758
Stuart D. Bale https://orcid.org/0000-0002-1989-3596

References

Ball, L., & Melrose, D. B. 2001, PASA, 18, 361
Blake, J. B., Mauk, B. H., Baker, D. N., et al. 2016, SSRv, 199, 309
Burch, J. L., Moore, T. E., Torbert, R. B., & Giles, B. L. 2016, SSRv, 199, 5
Decker, R. B. 1992, in AIP Conf. Proc. 264, Particle Acceleration in Cosmic Plasmas (Melville, NY: AIP), 183
Desai, M. I., & Giacalone, J. 2016, LRSP, 13, 3
Drury, L. 1983, RPPh, 46, 973
Fisk, L. A. 1971, JGR, 76, 1662
Fuselier, S. A., Lewis, W. S., Schiff, C., et al. 2016, SSRv, 199, 77
Gosling, J. T., Thomsen, M. F., Bame, S. J., & Russell, C. T. 1989, JGR, 94, 10011
Hellinger, P. 2003, P&SS, 51, 649
Kallenrode, M. B. 2013, Space Physics: An Introduction to Plasmas and Particles in the Heliosphere and Magnetospheres (3rd ed.; Berlin: Springer)
Koval, A., & Szabo, A. 2008, JGRA, 113, A10110
Krauss-Varban, D., & Wu, C. S. 1989, JGR, 94, 15367
Lepping, R. P., Acuna, M. H., Burlaga, L. F., et al. 1995, SSRv, 71, 207
Lin, R. P., Anderson, K. A., Ashford, S., et al. 1995, SSRv, 71, 125
Maksimovic, M., Zouganelis, I., Chaufray, J.-Y., et al. 2005, JGRA, 110, A09104
Oka, M., Iii, L. B. W., Phan, T. D., et al. 2019, ApJ, 886, 53
Oka, M., Terasawa, T., Seki, Y., et al. 2006, GeoRL, 33, 24104
Pollock, C., Moore, T., Jacques, A., et al. 2016, SSRv, 199, 331
Qin, G., Kong, F.-J., & Zhang, L.-H. 2018, ApJ, 860, 3
Russell, C. T., Hoppe, M. M., Livesey, W. A., Gosling, J. T., & Bame, S. J. 1982, GeoRL, 9, 1171
Schwartz, S. J. 1998, in Analysis Methods for Multi-Spacecraft Data, ed. G. Paschmann & P. W. Daly (Noordwijk: ESA), 249
Shimada, N., Terasawa, T., Hoshino, M., et al. 1999, Ap&SS, 264, 481
Szabo, A. 1994, JGR, 99, 14737
Tao, J., Wang, L., Zong, Q., et al. 2016, ApJ, 820, 1
Torbert, R. B., Russell, C. T., Magnes, W., et al. 2016, SSRv, 199, 105
Tsurutani, B. T., & Lin, R. P. 1985, JGR, 90, 1
Van Nes, P., Reinhard, R., Sanderson, T. R., et al. 1984, JGR, 89, 2122
Wang, L. 2009, PhD thesis, Univ. California, Berkeley
Wang, L., Lin, R. P., Salem, C., et al. 2012, ApJL, 753, L23
Wang, L., Yang, L., He, J., et al. 2015, ApJL, 803, L2
Wu, C. S. 1984, JGR, 89, 8857
Yang, L., Wang, L., Li, G., et al. 2018, ApJ, 853, 89
Yang, L., Wang, L., Li, G., et al. 2019, ApJ, 875, 104